

PHYSICAL REVIEW A

GENERAL PHYSICS

THIRD SERIES, VOLUME 39, NUMBER 12

JUNE 15, 1989

Formation of the negative muonium ion and charge-exchange processes for positive muons passing through thin metal foils

Y. Kuang, K.-P. Arnold,* and F. Chmely
Yale University, New Haven, Connecticut 06511

M. Eckhause
College of William and Mary, Williamsburg, Virginia 23185

V. W. Hughes
Yale University, New Haven, Connecticut 06511

J. R. Kane
College of William and Mary, Williamsburg, Virginia 23185

S. Kettell
Yale University, New Haven, Connecticut 06511

D.-H. Kim and K. Kumar
Syracuse University, Syracuse, New York 13210

D. C. Lu, B. Matthias, B. Ni, and H. Orth[†]
Yale University, New Haven, Connecticut 06511

G. zu Putlitz
University of Heidelberg, Heidelberg, Federal Republic of Germany

H. R. Schaefer
Yale University, New Haven, Connecticut 06511

P. A. Souder
Syracuse University, Syracuse, New York 13210

K. Woodle
Yale University, New Haven, Connecticut 06511
(Received 27 January 1989)

The negative muonium ion, $\text{Mu}^- \equiv \mu^+ e^- e^-$, has been produced by double electron pickup as a beam of positive muons passes through thin foils of various materials. The Mu^- ions were detected by electrostatically accelerating and analyzing the ions in a magnetic time-of-flight spectrometer. Yields of Mu^- , Mu and μ^+ as well are reported when μ^+ with kinetic energies from 380 to 800 keV impinge on thin Be, Al, and Au foils. A Monte Carlo simulation provides good agreement with the experimental results.

I. INTRODUCTION

Many experimental and theoretical studies have been done on charge-changing processes.¹⁻³ Naturally, the most extensively studied species have been the ions of hydrogen. In contrast, little experimental data are available

concerning charge capture by muons from solids.

The muonium ions ($\text{Mu}^+ \equiv \mu^+$, $\text{Mu} \equiv \mu^+ e^-$, and $\text{Mu}^- \equiv \mu^+ e^- e^-$) can be thought of as light isotopes of the hydrogen ions. They are of special interest, because they are purely leptonic and can be used for sensitive tests of quantum electrodynamics (QED). The neutral

muonium atom was recently produced in vacuum by a beam-foil method.⁴ Since then great effort has been devoted to measuring the Lamb shift of the muonium atom in the $n = 2$ state.^{5,6} With the discovery⁷⁻⁹ of the negative muonium ion Mu^- , another simple three-body system, besides H^- and the negative positronium ion Ps^- , is available for spectroscopy and collision studies.^{10,11} Since all these experiments require an intense source of muonium in a vacuum environment, it is important to study the production process itself.

The interaction of charged particles with matter is also of fundamental interest. At the velocity region at and below the maximum of the stopping power, the charge-exchanging processes become important. They contribute to the phenomena of energy loss and multiple scattering. However, the processes are not well understood. Careful experimental studies are very valuable for better understanding of the process. In this paper we expand on our earlier report⁹ about the formation of the negative muonium ion, and present our measurements of the yields of all muonium ions together with Monte Carlo simulations when positive muon beams of 380–800 keV kinetic energy (momenta of about 9–13 MeV/ c) passed through thin metal foils.

II. CHARGE-TRANSFER PROCESSES

It has long been recognized that charge-transfer processes, which have been studied by many experimentalists and theorists,¹⁻³ play an important role in atomic collisions and processes in complex atomic systems. In particular, a great deal of work has been done on hydrogen passing through gaseous targets. A proton traveling through a gas undergoes electron-capture and -loss processes. After a certain distance of travel, equilibrium is reached. For a three-component system, such as H^- , H^0 , and H^+ , there are six charge-changing processes. The equilibrium charge fraction can then be computed using the cross sections for the six processes.

The electron-capture processes of a proton in solids is much more complicated. The three charge states for hydrogen ions from solids were first studied experimentally by Phillips.¹² The experiment was repeated with a deuterium beam.¹³ The general observations of the charge-capture processes are that the fraction of a charge state is (i) strongly dependent on the velocity of the projectile, (ii) weakly dependent on the target material, and (iii) independent of the mass of the projectile. Therefore, a velocity scaling rule can be applied, i.e., the charge fraction for a muon is the same as that for a proton at the same velocity. This scaling rule has been verified down to 4 keV/amu in both transmission experiments^{12,13} and backscattering experiments^{14,15} in which the charge fractions of reflected particles were measured.

Based on the proton data,¹² the fractions of the charge state for muonium ions emerging from a solid foil can be plotted as a function of the energy, as shown in Fig. 1. Most of the neutral muonium atoms have less than 20 keV kinetic energy, while the fraction of the negative muonium ions becomes significant only for kinetic energies below 5 keV. The integrated rate of production of

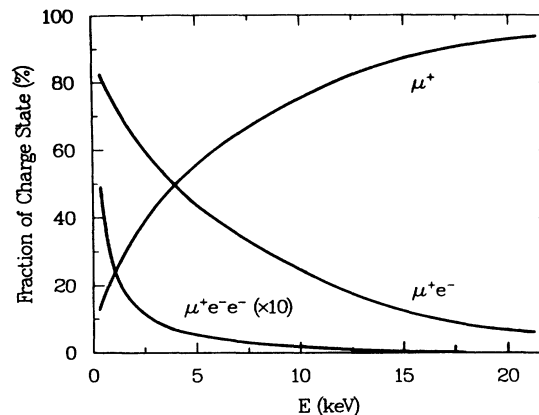


FIG. 1. Charge fractions of emerging muonium ions as a function of kinetic energy of emerging ions for μ^+ incident on a foil. Data are obtained by velocity scaling the proton data.

the negative muonium ions is about 2 orders of magnitude lower than that of the neutral muonium atoms.

It appears that the conventional description of the charge-state equilibrium of particles at higher velocities ($> Z^{2/3}v_0$, where v_0 is the Bohr velocity of 2.2×10^8 cm/sec) in gases can be adapted to solids. At these velocities, the capture and loss processes are due to the interaction with the inner shells of the target atom. A particle experiences electron-capture and -loss processes as it travels through a solid. The equilibrium of the charge state is reached after some number of collisions. The charge-state fractions can then be obtained by using cross sections computed for gaseous targets. This picture has been successfully used to describe the neutral fraction emerging from solid carbon with an incident proton beam.¹⁶ Since the fraction of the negative ions is negligible at these velocities, a two-component system, i.e., positive and neutral charge states, is assumed.

The concept of capture and loss inside the solid may be meaningless for velocities below the Fermi velocity of the electrons in a solid. (A typical Fermi velocity in a metal is about the same as the Bohr velocity v_0 .) Because of the collective screening by the target electrons in the metal and collision-broadening effects, there is no bound state in a metal.¹⁷ Therefore interactions at the surface, where screening is less effective and processes such as Auger neutralization, resonance neutralization, resonance ionization, and recombination can take place, become important.^{18,19} However, due to the complexity of the processes, there is no single theory that can explain all the experimental data.

At low velocities ($\leq v_0$) double-charge capture becomes significant. The fraction of negative ions increases monotonically with decreasing energy down to 4 keV/amu.^{12,13} In fact, it was found that the fractions of H^0 and H^- depend exponentially on energy in the region from 30 to 340 keV.²⁰ The processes were also studied in a backscattering experiment for energies below 4 keV/amu.²¹ As the energy decreases, double-charge capture reaches a maximum at about 3 keV/amu for most of

the metallic surfaces. A strong correlation between the work function of the target material and the formation of negative ions was observed.²² As the work function decreases, the maximum of the charged fraction moves towards lower energy and the amplitude of the maximum increases. The theories for the formation of negative ions at a surface were developed for alkali-covered surfaces. The general description is that a H^+ is first neutralized near the surface, then captures another electron at some distance from the surface. It may then lose an electron by resonance neutralization.²³ However, this picture cannot be applied directly to other metal surfaces,²¹ and at present there is no reliable theory for the formation of negative ions in beam-foil experiments.

III. APPARATUS AND PROCEDURE

The experiment described here employed the beam-foil method and used a separated subsurface beam of positive muons. The stopped muon channel (SMC) at the Clinton P. Anderson Meson Physics Facility at Los Alamos National Laboratory (LAMPF) was tuned to a low-momentum subsurface μ^+ beam,²⁴ such that the peak of the stopping profile was centered near the downstream surface of the production foil. The experimental apparatus is shown in Fig. 2. The muon beam passed through a thin scintillator and a 0.2-mg/cm² aluminum protection foil which prevented sparking at high voltage. The production foil was mounted on the high-voltage end of an electrostatic accelerator column capable of operation up to ± 25 kV, while a highly transparent copper mesh (90% transmission) held at ground potential maintained a uniform accelerating field. Three different foils were used as charge-exchange media. The particles were selected for charge state and momentum by a wedge-shaped 60° bending magnet with double-focusing properties symmetric about the central trajectory of the particles. A solenoid of 130 cm length transported the ions away from the direct beam into a background-reduced re-

gion. As a result of its fringe fields, this solenoid focused the beam onto a microchannel plate (MCP) detector. The decay positrons from muons were observed in either of two pairs of scintillator telescopes installed above and below the MCP. The characteristic Michel energy spectrum of the positrons from μ^+ decay was measured with a NaI(Tl) detector. Neutral muonium atoms were also collected downstream in the straight direction on a Teflon plate which subtended a solid angle of about 10 msr at the production foil. The decay positrons from muons incident on the beam stop were observed with another NaI(Tl) detector. Time-of-flight spectra were taken with the muon counter (plastic scintillator), microchannel plate, and scintillator telescopes. The data were read into a Digital Equipment Corporation PDP-11/34 computer via a CAMAC interface. For this exploratory experiment, the design of the apparatus was a compromise of optimization of the signal rate for Mu^- and availability of components for the spectrometer.

A. Subsurface beam of positive muons

The subsurface μ^+ beam is highly polarized and has a duty factor of 6%, characteristic of the primary proton beam in the linear accelerator. An ($E \times B$) separator was used to reduce e^+ contamination of the μ^+ beam. Since the diffusion of radioactive gases in the channel created high background rates in the scintillator and MCP detector, a gas barrier of 1.5 μm Mylar was inserted in the beam line. The effect of the gas barrier was the following: It left the vacuum upstream at about 5×10^{-3} Torr, thus retarding the diffusion of the radioactive gases (^6He , ^{12}N) in the 30-m-long channel such that most decayed before reaching the barrier. The downstream vacuum was about 3×10^{-6} Torr. The 1.5- μm gas barrier itself could effectively prevent nitrogen from diffusing through. The beam-spot size of the downstream end of the channel was calculated to be about 5 cm full width at half maximum (FWHM) using the computer code TRANSPORT.^{25,26} The beam was collimated with 7-cm-thick Pb blocks, which had a circular opening of 7.6 cm in diameter, before it entered the apparatus.

The incident muon beam was monitored by a 2-mg/cm² plastic scintillator, which served both as a degrader and as a muon counter. This thin plastic scintillator from Nuclear Enterprises (NE102A) is essentially identical to that used in an experiment on formation of muonium in the $2S$ state and observation of the Lamb-shift transition.^{6,27} The detection efficiency of the muon counter was estimated to be $(97 \pm 1)\%$ for muons. An average flux of $140 \times 10^3 \mu^+/\text{sec}$ was obtained.

B. Production foils

As indicated in the proton experiments, the neutral and the negative fractions are almost independent of the foil material.¹² Since the atomic electrons in the foil have a typical velocity of v_0 , it is most probable for muons of similar velocity, i.e., a few keV of kinetic energy, to capture electrons in the foil. In order to maximize the number of muonium atoms and negative muonium ions pro-

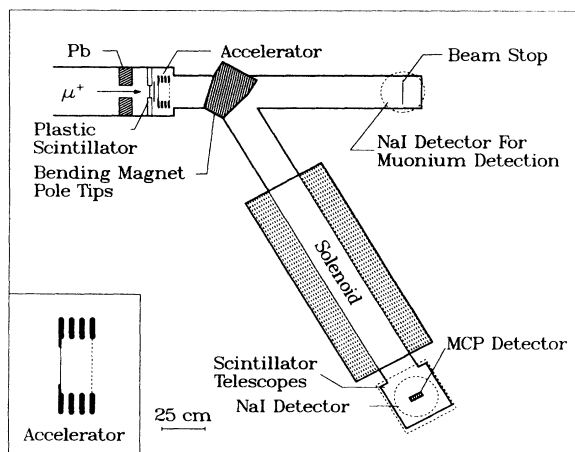


FIG. 2. Schematic diagram of the experimental apparatus for observation of the charge states of the outgoing beams from positive muons passing through a thin foil.

duced, it is necessary to have as little material as possible in the beam, thus allowing the use of a low-momentum beam of small range straggling and high stopping density.

Since energy loss^{28–30} and multiple scattering^{31–33} are strongly Z dependent, it is interesting to investigate these effects with foils of different atomic numbers. The foils used were beryllium ($Z=4$), aluminum ($Z=13$), and gold ($Z=79$). Their properties and thicknesses are listed in Table I. The momentum of the μ^+ beam was tuned to accommodate the different thicknesses of the foils. By tuning the beam momentum in steps of 0.25 MeV/ c , the muonium rate in the straight channel was optimized for the Al foil. For the Be and Au foils, the beam momenta were chosen on the basis of range and energy-loss calculations such that the centroids of the energy distributions of the outgoing muons would be close to that for the Al foil.

C. Magnetic spectrometer

The design of the transport system for low-energy positive muons or negative muonium ions is based on calculations using the computer code TRANSPORT. The beam envelope is computed, assuming a phase space of $\sigma_x\sigma_{x'}=\sigma_y\sigma_{y'}=4\text{ cm}\times 200\text{ mrad}$ and a momentum spread of $\pm 5\%$ at 2 MeV/ c central momentum after the accelerator stage. The bending magnet, shown in Fig. 2, served as both a charge and a momentum selector. Particles with the appropriate sign of charge and momentum were deflected by 60° . Since the beam intensity of the negative muonium ions is very low, it is desirable to use a wedge magnet with double-focusing effect.^{34,35} TRANSPORT calculations show that a wedge magnet of “effective” 28° will give the best focusing effect in both the horizontal and the vertical planes. Therefore, an H -frame magnet with pole pieces forming a 28° wedge was used. A Monte Carlo calculation shows that the magnet has a momentum acceptance of about 30% (FWHM). The bending radius is 22.7 cm. Because of limitation in space, the optimum double-focusing condition was not used. However, the system results in a symmetric beam envelope in the horizontal and the vertical planes according to TRANSPORT calculations.

As is well known, the fringe field of a solenoid can provide focusing for a charged-particle beam. Unlike a quadrupole magnet, a solenoid has no defocusing effect. It is therefore preferable to use a solenoid as a focusing element for a low-energy beam. The coils of the solenoid are made of 2.54-cm-wide and 50.8- μm -thick Al strips. They have an inner diameter of 28.7 cm and an outer diameter of 39.1 cm and they are 128.9 cm long. Cooling

TABLE I. Properties and thicknesses of foils used as charge-capture media in the experiment.

Foil	Z	A	Density (g/cm^3)	Thickness (μm)
Be	4	9.01	1.848	24.9
Al	13	26.98	2.70	0.8
Au	79	196.97	19.32	2.0

water flows through two sets of copper tubing between the vacuum pipe and the coils. The entire solenoid was covered with a cylindrical tube of 0.95-cm-thick iron and the two ends were covered with 0.95-cm-thick plates of iron which provided a return path for the magnetic field. The field along the axis was mapped and found to be in good agreement with a POISSON^{36,37} calculation. The effective length was measured to be 135 cm. In the experiment the solenoid was set at $713\pm 5\text{ G}$, which was the largest field obtainable without overheating the magnet.

A computer simulation of the momentum acceptance of the solenoid is shown in Fig. 3. The momentum acceptance at $p=2\text{ MeV}/c$ with a detector of 75 mm diameter is about 8.5% (FWHM), which is much smaller than the acceptance of the bending magnet. The peaks at 2 and 3.2 MeV/ c are relevant to our experiment. As will be shown later, in the experiment we observed the peak at 2 MeV/ c and part of the peak at 3.2 MeV/ c in the time-of-flight measurements. The transport efficiency of the whole system including the accelerator is about 10%, depending on the distribution of the particles, as calculated from the Monte Carlo code.

D. Energy spectra of decay positrons

With a maximum obtainable field of 1.1 kG in the bending magnet, to sweep out charged particles, the rate of neutral muonium atoms was measured at the Teflon beam stop at the end of the straight channel. The Michel energy spectrum of positrons from muon decay was measured with the NaI crystal scintillator. The positrons have energies from 0 to 53 MeV with a maximum range of about 5 cm in the NaI. The NaI(Tl) crystal is a cylinder 25 cm in diameter and 25 cm high. The scintillator light was viewed by seven 5 cm-diam photomultiplier tubes with the gains adjusted to be equal.

A block diagram of the logic for measuring the Michel spectrum is shown in Fig. 4. A scintillator telescope con-

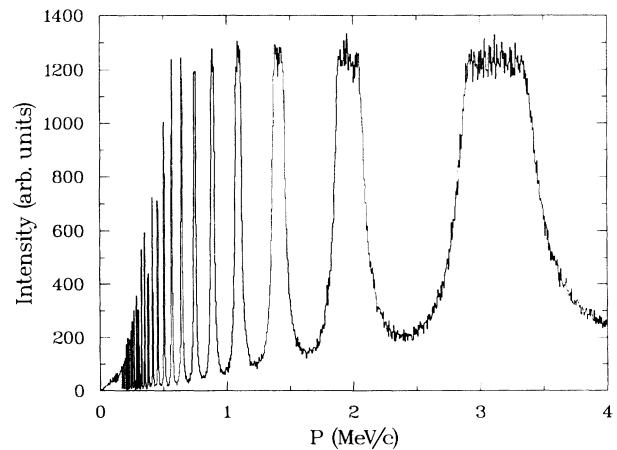


FIG. 3. Momentum acceptance of the solenoid based on Monte Carlo simulation. A point source located 40 cm upstream of the solenoid is assumed. The MCP detector of 7.5 cm diameter is located 25 cm downstream of the solenoid. The magnetic field is 712.5 G.

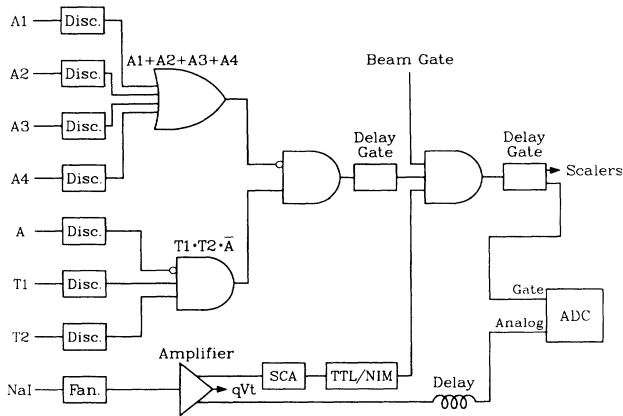


FIG. 4. Logic diagram of electronic setup for measuring the Michel spectrum in the straight channel.

sisting of two circular plastic scintillators, $T1$ and $T2$, of 0.5 cm thickness and 6 cm radius, was placed between the beam stop and the NaI crystal. The telescope subtended a fractional solid angle of 2.9% at the center of the beam stop in the straight channel. An anticoincidence counter A ($30 \times 30 \times 0.8$ cm³) located above the beam stop was used to veto signals from cosmic rays. The NaI was also surrounded by a veto shield consisting of four plastic scintillators, $A1$, $A2$, $A3$, and $A4$, each of them bent to form a quarter of a cylinder. Lead bricks surrounded this anticoincidence shield, which had an efficiency of about 95%.

The Michel spectrum of decay positrons from muons was measured with the NaI detector located downstream in the straight channel by turning off the bending magnet and thus bringing positive muons into the detector. A typical spectrum is shown in Fig. 5. The energy calibra-

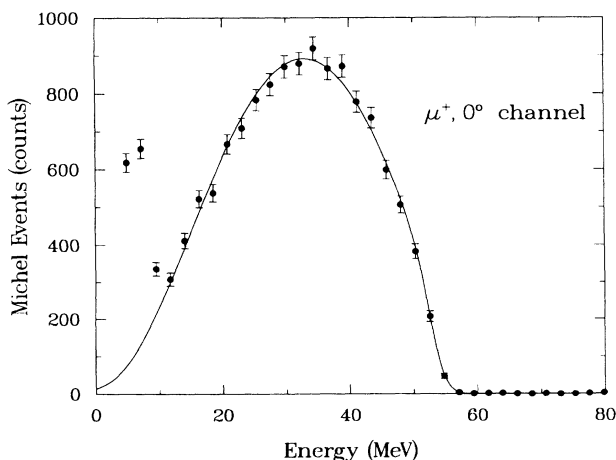


FIG. 5. Michel spectrum taken with positive muons in straight direction in Fig. 2 for energy calibration of the NaI detector.

tion consists of fitting the pulse-height distribution to the Michel spectrum, taking into account the detector resolution and geometry. The energy resolution was found³⁸ to be $22\%/E^{1/4}$ (FWHM), where E is in MeV. The beam-related background, as, for example, from beam positrons, dominates the region of the spectrum below 20 MeV. With maximum field strength in the bending magnet, positive muons were swept out, leaving only neutral muonium atoms entering the channel downstream of the bending magnet. The radius of curvature of a charged particle of 10 MeV/ c momentum is about 30 cm in this field. The number of decay positrons detected by the NaI scintillator is determined by setting a window in the spectra of the amplitude-to-digital converter (ADC) from channel 160 to channel 360, which corresponds to 66% of the full Michel spectrum. A flat background rate based on the data from channel 500 to channel 800 in the ADC spectrum was subtracted from the data in the window. The rate of muonium atoms incident at the beam stop was calculated from the number of decay positrons observed.

E. Time-of-flight measurements

The time of flight (TOF) of the charged particles was measured with the muon counter (plastic scintillator) and the MCP detector. The latter served as both a beam stop and a detector for μ^+ and Mu^- transported through the 60° channel. The MCP is a pair of microchannel plates in which the channel axes of the two plates are tilted by 16° with respect to one another in order to eliminate spurious noise caused by positive-ion feedback.³⁹ It is a Chevron channel electron multiplier array (Model No. 3075) manufactured by Galileo Electro-Optics Corp. with an active diameter of 75 mm. A grounded mesh (95% transparent) was mounted in front of the MCP. The MCP was operated at 815 V per plate with no interplate bias voltage. This mode of operation helped to discriminate muons from positrons which we found produce considerably smaller pulses than do muons.⁴⁰ The detection efficiency of a MCP has been studied⁴¹ with H^+ , He^+ , and O^+ in the energy region of several keV. An efficiency of $(65 \pm 10)\%$ is expected for muons, although no direct measurement is available.

Two pairs of scintillators, $C1, C2$, and $C3, C4$, were mounted, respectively, above and below the MCP to detect the decay positrons from muons or negative muonium ions stopped in the MCP. These scintillators are essentially identical to the scintillator A described above. They subtended a fractional solid angle of 16.2% at the MCP. The logic diagram for the scintillator telescopes is shown in Fig. 6. The signature of a muon or of a negative muonium ion incident on the MCP was defined as a delayed coincidence of the signal from the MCP and a 4.2- μsec gate, $(C12 + C34) \cdot \text{BEAM}$, shown in Fig. 6. Decay positrons from muons stopped in the MCP detector were observed in the time interval from 0 to 3.3 μsec . This coincidence signal is denoted as the START to the time-to-digital converters (TDC's) shown in Fig. 7. One of the TDC's measured the muon lifetime and the other the time of flight of muons or negative muonium

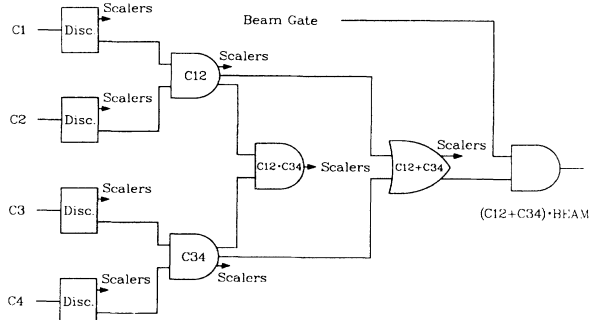


FIG. 6. Logic diagram of the scintillator telescopes for detecting decay positrons in the 60° channel.

ions from the muon counter to the MCP. The delayed and beam-gated (C12+C34) signal served as a STOP in the measurement of the muon lifetime. For this we used a LRS model no. 2228A TDC, modified to have about a 5- μ sec range, with a channel width of 2.5267 ± 0.0008 nsec.

An EG&G model no. TD104 TDC was used for the time-of-flight measurements. The signal from the muon counter, which came from a three-out-of-four coincidence of the phototubes coupled to the scintillator, $\mu_{3/4}$, was delayed by about 1 μ sec. The time-of-flight was measured in reversed timing, since the instantaneous counting rate of the MCP was less than 200 sec^{-1} , which was significantly lower than the instantaneous rate of the muon counter of $2.3 \times 10^6 \text{ sec}^{-1}$. The logic, shown in Fig. 7, was set up in a cascading fashion to allow three stop signals, STOP1, STOP2, and STOP3, corresponding to three hits in the muon counter for each MCP signal. This TDC was also modified so that it had about 1 μ sec full range. Typical TOF spectra of the muons are shown in Fig. 8. The TDC gain (0.999 ± 0.001 nsec/channel) was calibrated with a frequency synthesizer. The relation between the time-of-flight and the channel number in the

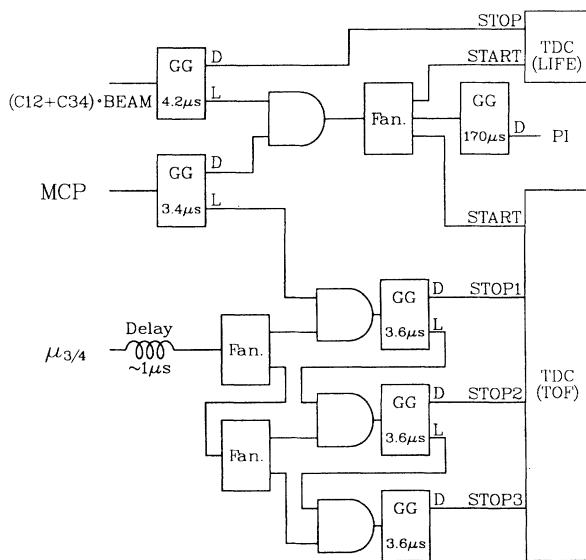


FIG. 7. Logic diagram of electronic setup for muon-lifetime and time-of-flight measurements.

EG&G TD104 TDC, obtained using a pulser, is

$$t_{\text{TOF(nsec)}} = 916 - 0.999n_{\text{TDC}} \pm 20, \quad (1)$$

where t_{TOF} is the time-of-flight of a particle from the muon counter to the MCP and n_{TDC} is the channel number in the TDC. The 20-nsec uncertainty is due to the absolute time calibration.

The field of the bending magnet was first tuned to maximum transmission for positive muons. The voltage of the accelerator stage was varied to accelerate low-energy positive muons in accordance with the momentum tune of the channel. Negative muonium ions were studied by reversing the polarities of the accelerating voltage and the field in the bending magnet. The data were sent to a PDP-11/34 computer and written to magnetic tape. The data analysis was done on a VAX/VMS computer.

IV. OBSERVATIONS AND RESULTS

The formation of neutral muonium atoms was observed with the NaI detector in the straight channel. As pointed out in Sec. II, the electron-capture probability is very sensitive to the velocity of the incident muon. In order to maximize the capture probability, the momentum of the incident muon beam was tuned by varying the set-

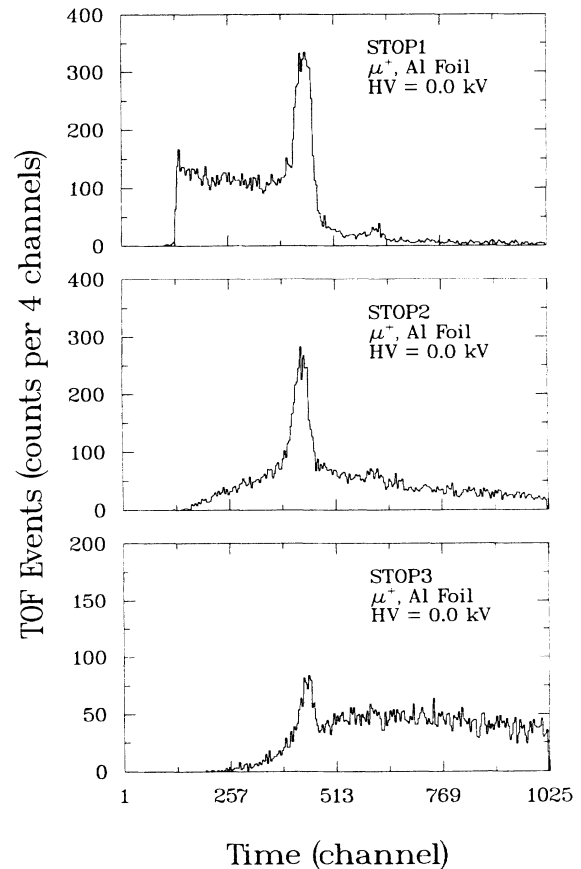


FIG. 8. TDC spectra of the time-of-flight of positive muons taken with Al foil and accelerator voltage set to 0.0 kV.

tings of the SMC magnets. After optimizing the momentum of the incident beam, we studied the characteristics of the low-energy positive muons and the negative muonium ions emerging from the foil. The times of flight of both the positive muons and the negative muonium ions through the 60° channel were measured. From the resulting spectra one can compute the masses of the particles. The fact that the negatively charged particles contain muons was verified by measuring both the lifetime of the particles and the characteristic Michel spectrum of the decay positrons from positive muons.⁹ In this section the experimental data and results will be presented.

A. Muonium atoms

The initial stage of the experiment was a search for neutral muonium atoms with the Al production foil in place. The momentum of the incident μ^+ beam was tuned in order to optimize the rates. The rates in the NaI and projected rates of muonium atoms at the beam stop are listed in Table II. The number of incident muons μ_{inc}^+ (also in Table II) is given by

$$\mu_{\text{inc}}^+ = \frac{(\mu_{3/4})_{\text{gated}} t_{\text{ungated}} - (\mu_{3/4})_{\text{ungated}} t_{\text{gated}}}{t_{\text{ungated}} - t_{\text{gated}}}, \quad (2)$$

where t is the experimental running time and the subscripts *gated* and *ungated* denote beam-gated and not-beam-gated counts, respectively. The observed muonium rates at the beam stop are plotted as solid circles with error bars in Fig. 9(a) against the momentum of the incident muon beam. The maximum rate is at about 9.75 MeV/c. A similar measurement was also done with a Au foil; for this foil, the incident muon beam was tuned to 10.67 MeV/c momentum at which the average rate of incident muons was $140 \times 10^3 \text{ sec}^{-1}$. The result is also given in Table II. The momenta of the incident muon beams were calibrated using the time-of-flight technique in an auxiliary experiment and the uncertainty of the beam momentum is expected to be $\pm 5\%$. The systematic error in computing the projected rates of the muonium atoms at the beam stop is about $\pm 10\%$ with comparable contributions from the uncertainties in the detection efficiency of the scintillator telescope and the solid angle.

B. Positive muons

The TDC spectra shown in Fig. 8 for positive muons are distorted due to the high counting rate in the muon counter. However, the spectrum for correlated events can be obtained by using the following iterative expression:

$$S(t_i) = \frac{1}{1 - U\Delta t} \left[M_1(t_i) e^{-Ut_i} - NU + U \sum_{j=0}^{i-1} S(t_j) \Delta t \right], \quad (3)$$

$$t_j = j\Delta t, \quad j = 0, 1, 2, \dots \quad (4)$$

where $M_1(t)$ is the first TDC spectrum STOP1, N is the total number of measurements, i.e., number of STARTs, U is the instantaneous counting rate of the muon counter, and Δt is the time interval of one channel of the TDC, which is about 1 nsec. The detailed derivation of Eq. (3) is given in the Appendix. Figure 10 shows the spectrum $S(t)$ by solid circles with error bars. Another method for obtaining the undistorted distribution is to require no more than one count in some time window. One such spectrum is also shown in Fig. 10 as a histogram, normalized to the same peak height as that of $S(t)$. In a case like ours, where most events fall into a peak region, the window approach is fully adequate, but the method outlined above is applicable more generally. In Fig. 10, the main peak at channel 444 corresponds to about 2 MeV/c in momentum and the small peak at channel 630, which is also due to the focusing effect of the solenoid, corresponds to 3.2 MeV/c.

From the undistorted time-of-flight spectra of Eq. (3), the number of muons stopped by the MCP detector can be computed. The spectra are divided into two regions. The number of counts was computed by integrating the spectra over time from channel 339 to channel 538. A flat background computed by integrating the spectra over time from channel 141 to channel 338 was subtracted from each spectrum.

The counting rates of the scintillator telescopes with the Al foil at various accelerating voltages are listed in Table III, together with the projected rates at the focal plane where the MCP detector was located. The projected rates were computed by taking into account the detec-

TABLE II. Average rates of μ_{inc}^+ , rates in NaI, and projected rates of muonium atoms at the beam stop. Errors, given in parentheses, are statistical only.

Foil	P_μ (MeV/c)	μ_{inc}^+ rate (10^3 sec^{-1})	Rate in NaI ($10^{-7}/\mu_{\text{inc}}^+$)	Projected rate at beam stop ($10^{-5}/\mu_{\text{inc}}^+$)
Al	9.02	80	2.75(28)	1.44(15)
	9.49	106	8.88(37)	4.64(19)
	9.75	122	10.24(41)	5.35(21)
	10.00	99	9.92(38)	5.18(20)
	10.25	117	8.20(40)	4.29(21)
Au	10.67	140	3.18(18)	1.66(9)

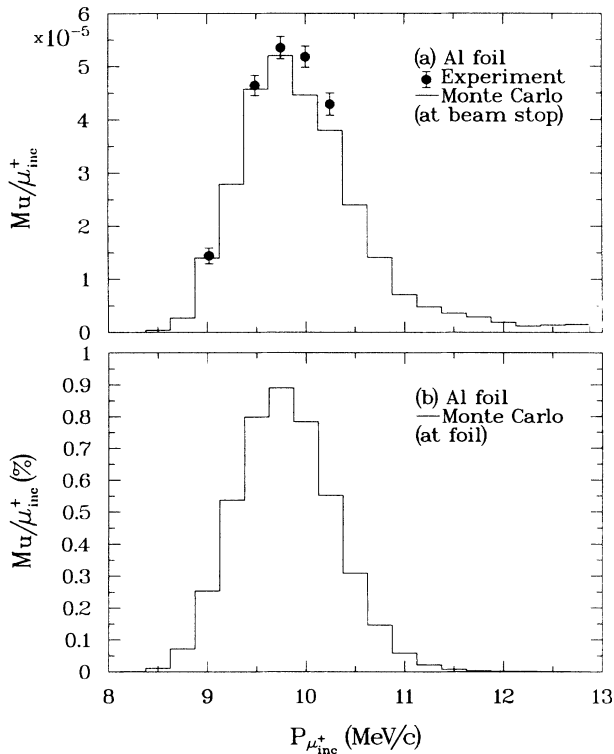


FIG. 9. Muonium rates (a) at the beam stop and (b) at the production foil. The solid circles with error bars are the experimental data as given in Table II. The histograms represent Monte Carlo simulations. The production foil is 0.8- μm -thick Al. Errors are statistical only.

tion efficiency of the scintillator telescope (90%), the time window of the telescope (3.3 μsec corresponding to 77.9%), the fractional solid angle subtended by the telescope (16.2%), and the detection efficiency of the MCP detector (65%). The central momentum of the incident muon beam for the Al foil was 9.75 MeV/c. The systematic errors in computing the projected rates are about

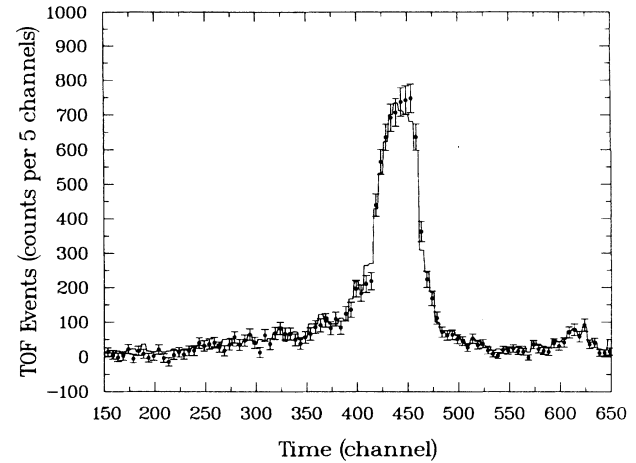


FIG. 10. Time-of-flight spectrum of the correlated events corresponding to the spectra in Fig. 8. Data points with statistical errors are evaluated according to the method described in the Appendix. The histogram corresponds to data derived according to the window method.

$\pm 20\%$, where the largest contribution comes from the uncertainty in the detection efficiency of the MCP detector.

The results of the measurements on the low-energy muons performed with the Be foil and the Au foil are listed in Tables IV and V, respectively. The Be data were taken with a 12.63-MeV/c incident muon beam, while a 10.67-MeV/c muon beam was used for the Au foil.

C. Negative muonium ions

The data taken with negative muonium ions were analyzed using the same method as for positive muons. Table VI lists the rates of the negative muonium ions at various accelerating voltages with the Al foil. An incident muon beam of 9.75 MeV/c momentum was used for these measurements. Here the same consideration with respect to the systematic errors applies as in Sec. IV B.

TABLE III. Average rates of μ_{inc}^+ , telescope rates, and projected rates of low-energy positive muons at the focal plane taken with the Al foil at various accelerating voltages. The momentum of the incident muon beam was 9.75 MeV/c. Errors, given in parentheses, are statistical only.

Accelerating voltage (kV)	μ_{inc}^+ rate (10^3 sec^{-1})	Telescope rate ($10^{-6}/\mu_{inc}^+$)	Rate at focal plane ($10^{-6}/\mu_{inc}^+$)
21.0	132	0.8(3)	10.8(40)
20.0	104	3.2(3)	43.5(39)
19.0	132	4.7(3)	63.5(36)
18.0	133	7.9(3)	106.9(37)
15.0	129	10.0(4)	134.7(56)
12.0	132	11.0(5)	148.5(62)
6.0	121	12.8(9)	164.1(123)
0.0	121	11.2(2)	151.6(29)
-24.2	114	13.0(6)	175.4(74)

TABLE IV. Average rates of μ_{inc}^+ , telescope rates, and projected rates of low-energy positive muons at the focal plane taken with the Be foil at various accelerating voltages. The momentum of the incident muon beam was 12.63 MeV/c. Errors, given in parentheses, are statistical only.

Accelerating voltage (kV)	μ_{inc}^+ rate (10^3 sec^{-1})	Telescope rate ($10^{-6}/\mu_{\text{inc}}^+$)	Rate at focal plane ($10^{-6}/\mu_{\text{inc}}^+$)
21.0	125	0.6(1)	7.4(18)
20.0	127	1.2(1)	15.8(19)
19.0	125	1.6(2)	21.3(24)
17.0	110	4.0(2)	53.9(29)
15.0	125	5.7(3)	77.2(37)
10.0	130	6.2(3)	83.4(45)
6.0	128	6.4(4)	86.6(55)
0.0	130	6.6(3)	89.1(47)

The results on negative muonium ions measured with the Be and Au foils are listed in Tables VII and VIII, respectively. The incident-muon-beam momenta are 12.63 MeV/c for the Be foil and 10.67 MeV/c for the Au foil.

The observation of the negative muonium ion was verified by measuring the time and energy spectra of the decay positrons from muons and by measuring the mass of the ion using a time-of-flight technique.⁹ With a mass of 106.7 MeV/c² for the negative muonium ion, the estimated centroid of the energy distribution has a relatively large error due to the 20-nsec uncertainty in the time calibration [see Eq. (1)]. However, the TDC gain was calibrated very precisely. We also took time-of-flight spectra of the negative muonium ions with a different tune of the spectrometer by scaling down the settings. From the differences of the time of flight at low channel settings and at high channel settings, the ambiguity in the time calibration can be eliminated from the estimate of the centroid. A more precise value compared to that reported before⁹ for the centroid of the Mu^- energy distribution of 0.2(1) keV is obtained, which is consistent with values obtained for negative hydrogen ions.

V. DISCUSSION AND SUMMARY

Because of the complicated nature of the transport system employed in the experiment, it is desirable to have a Monte Carlo simulation for the system. A Monte Carlo computer code was therefore developed.⁴⁰ The program simulates the processes of energy loss and straggling of positive muons, and charge capture by positive muons based on the data from hydrogen, and of multiple scattering. It can also be used as a ray-tracing program for the transport system. We have successfully used this program to simulate our experimental results.

A. Muonium atoms

For the given amount of material in the beam with the Al production foil, the formation fraction of muonium atoms peaks at an incident momentum of about 9.75 MeV/c, as shown in Fig. 9(a). This is in very good agreement with the Monte Carlo simulations, presented in Fig. 9(a) as a histogram. The Monte Carlo simulations also give predicted muonium rates at the Al foil, as shown in

TABLE V. Average rates of μ_{inc}^+ , telescope rates, and projected rates of low-energy positive muons at the focal plane taken with the Au foil at various accelerating voltages. The momentum of the incident muon beam was 10.67 MeV/c. Errors, given in parentheses, are statistical only.

Accelerating voltage (kV)	μ_{inc}^+ rate (10^3 sec^{-1})	Telescope rate ($10^{-6}/\mu_{\text{inc}}^+$)	Rate at focal plane ($10^{-6}/\mu_{\text{inc}}^+$)
22.5	147	0.2(1)	1.9(9)
20.0	145	0.9(1)	12.7(18)
19.0	147	2.0(2)	27.5(27)
17.5	146	3.5(2)	47.4(34)
15.0	145	3.2(2)	43.4(28)
10.0	141	1.7(2)	23.6(23)
0.0	145	1.4(2)	19.5(20)

TABLE VI. Average rates of μ_{inc}^+ , telescope rates, and projected rates of negative muonium ions at the focal plane taken with the Al foil at various accelerating voltages. The momentum of the incident muon beam was 9.75 MeV/c. Errors, given in parentheses, are statistical only.

Accelerating voltage (kV)	μ_{inc}^+ rate (10^3 sec^{-1})	Telescope rate ($10^{-7}/\mu_{\text{inc}}^+$)	Rate at focal plane ($10^{-6}/\mu_{\text{inc}}^+$)
-14.00	137	3.24(78)	4.38(106)
-15.50	126	6.42(99)	8.67(134)
-17.00	129	10.40(41)	14.04(55)
-17.50	114	9.74(97)	13.14(130)
-17.75	105	8.90(65)	12.02(88)
-18.50	136	9.48(102)	12.80(138)
-20.00	133	4.13(89)	5.58(121)

Fig. 9(b). Figure 9(b) shows that the muonium-formation probability is slightly less than 1%. At the optimum momentum (9.75 MeV/c), our computer simulation shows that half of the incident muons are stopped in the material, indicating that the stopping distribution is centered at the exit surface of the production foil.

A similar simulation was performed for the Au foil. It gives a muonium rate of $1.33 \times 10^{-5}/\mu_{\text{inc}}^+$ at the beam stop and a muonium-formation probability of 1.8% at the foil. The fact that the rate at the beam stop for Au is lower than that for Al, while the formation fraction for Au foil is higher than that for Al, is due to a wider angular distribution of the muonium atoms from the Au foil. We will discuss this effect in more detail later.

B. Positive muons

We also simulated the results of the low-energy muons corresponding to our experimental data listed in Tables III–V taken at the end of the 60° channel. These are shown in Fig. 11. The solid circles with error bars represent the experimental data in Tables III–V. The simulations were performed in steps of 1 kV in the accelerating voltage and are plotted as histograms. They agree with the experimental data within a factor of 2.

The momentum and angular distributions of the positive muons exiting the production foils are also obtained by Monte Carlo simulations. The simulations are based on the experimental running conditions in which the central momenta of the incident muon beams are 9.75

MeV/c for the Al foil, 12.63 MeV/c for the Be foil, and 10.67 MeV/c for the Au foil. Results are shown in Figs. 12 and 13. It is evident in Fig. 13 that, as expected, the angular distribution widens with decreasing energy.

Figure 11 can be explained qualitatively as follows. The energy distribution of muons for the Be foil is peaked at higher energy than those for Al and Au foils (see Fig. 12). The muons from the Be foil are predominantly forwardly directed. However, because of a finite angular distribution, the transport efficiency of the spectrometer will decrease as the initial energy increases, i.e., as the accelerating voltage decreases. Therefore, the rate of detected muons does not increase as fast as the energy distribution of the muons at the foil. In fact, the rates saturate at about 10 kV accelerating voltage. On the other hand, there are more low-energy muons exiting from the Au foil than from the Al and Be foils. However, due to the much wider angular distribution (see Fig. 13), the number of muons transported to the MCP detector is reduced as reasoned above. The muons with very low energies are less affected by this reduction, since they are accelerated under higher voltage, and thus are more likely to be accepted by our apparatus. The net effect for Au is that we observed a maximum rate of muons transported to the detector at about 16–17 kV.

C. Negative muonium ions

The process of producing negative muonium ions can also be simulated with the Monte Carlo code. Again, an

TABLE VII. Average rates of μ_{inc}^+ , telescope rates, and projected rates of negative muonium ions at the focal plane taken with the Be foil at various accelerating voltages. The momentum of the incident muon beam was 12.63 MeV/c. Errors, given in parentheses, are statistical only.

Accelerating voltage (kV)	μ_{inc}^+ rate (10^3 sec^{-1})	Telescope rate ($10^{-7}/\mu_{\text{inc}}^+$)	Rate at focal plane ($10^{-6}/\mu_{\text{inc}}^+$)
-16.00	136	4.12(77)	5.57(104)
-17.50	145	4.21(80)	5.69(108)
-18.50	128	5.49(86)	7.41(116)
-19.00	139	4.84(80)	6.54(108)

TABLE VIII. Average rate of μ_{inc}^+ , telescope rate, and projected rate of negative muonium ions at the focal plane taken with the Au foil. The accelerator voltage was at -17.5 kV. The momentum of the incident muon beam was 10.67 MeV/c. Errors, given in parentheses, are statistical only.

Accelerating voltage (kV)	μ_{inc}^+ rate (10^3 sec^{-1})	Telescope rate ($10^{-7}/\mu_{\text{inc}}^+$)	Rate at focal plane ($10^{-6}/\mu_{\text{inc}}^+$)
-17.50	146	10.83(94)	14.6(13)

incident muon beam of 9.75 MeV/c momentum was used for the Al foil. The results of the simulations are shown in Fig. 14 as a histogram. The solid circles with error bars in the figure represent the data in Table VI. The fact that the width of the distribution (4.5 kV FWHM) is comparable to the acceptance of the channel suggests that the energy distribution of the negative muonium ions is narrow compared to 4.5 keV.

The results of the simulations for the Be foil and for the Au foil with acceleration voltage set to -17.5 keV are given in Table IX, where the momenta of the incident

muon beams were 12.63 MeV/c for the Be foil and 10.67 MeV/c for the Au foil. Based on these simulations, the projected formation fractions of negative muonium ions at the production foils can be obtained. They are listed in Table IX, together with some of the relevant experimental data.

With respect to the Mu^- formation probabilities, the results can be explained qualitatively as follows. The stopping density of the outgoing particles from the Be foil is relatively low. Hence, the formation fraction of the negative muonium ions is lower. In comparison, the en-

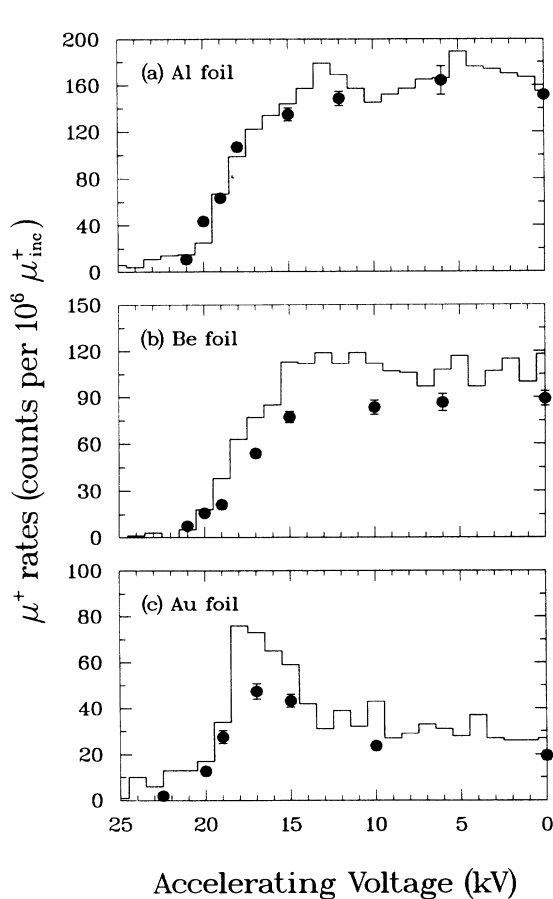


FIG. 11. Low-energy muon rates for different foils at the focal plane with various accelerating voltage. The solid circles with error bars represent projected rates based on time-of-flight data. The histograms correspond to Monte Carlo simulations.

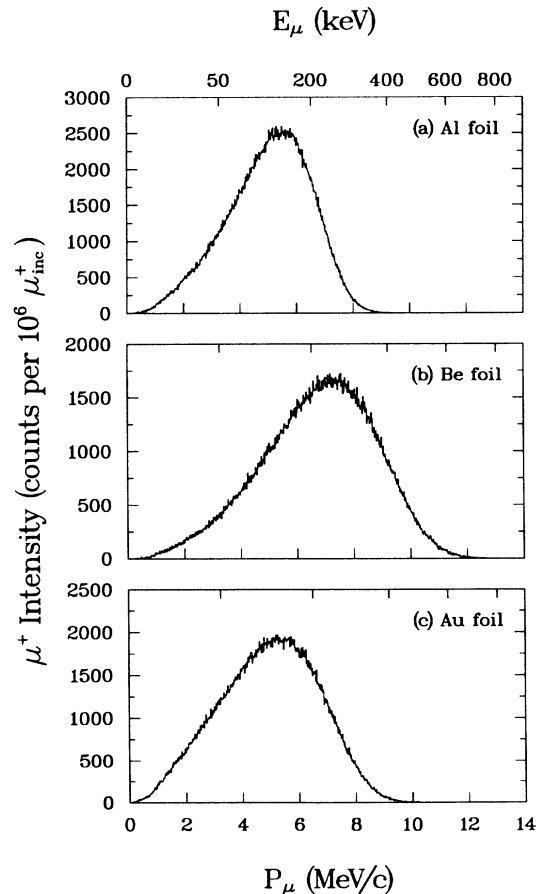


FIG. 12. Momentum distributions of outgoing positive muons from (a) Al foil, (b) Be foil, and (c) Au foil as calculated with the Monte Carlo code. The bin size is 20 keV/c. Upper tic marks represents the kinetic energy scale.

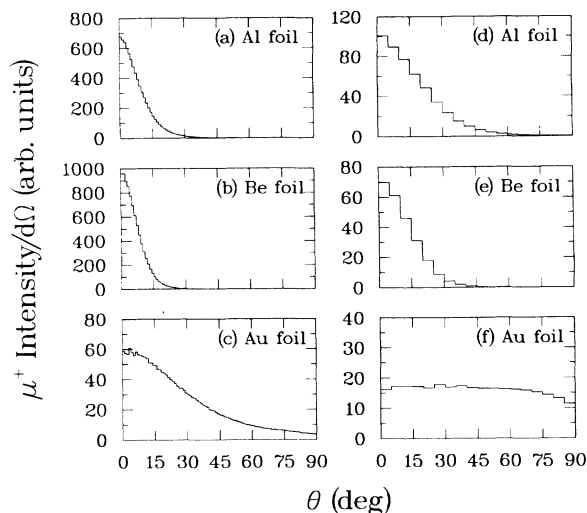


FIG. 13. Angular distributions of outgoing positive muons integrated over all energies from (a) Al foil, (b) Be foil, and (c) Au foil calculated with the Monte Carlo code. The bin size is 1° ; (d)–(f), same for outgoing positive muons with an energy range of 15–20 keV and a bin size of 5° .

ergy distribution of the outgoing particles from the Au foil is peaked at lower energy. Therefore, the formation fraction of the negative muonium ions is higher. Another interesting feature of the results in Table IX is that the collection efficiency of the negative muonium ions, defined as the ratio of the rate at the focal plane to the formation fraction, is not the same for these foils. This is in accordance with the general expectation of a wider angular distribution of outgoing particles from a foil with larger atomic number Z than that from a foil with smaller atomic number, due to multiple scattering. This might suggest the interesting possibility of achieving higher Mu yield from a composite target such as an Al foil coated with a thin layer of Au at the exit surface of the foil.

D. Summary

In conclusion, we have measured the yields of the muonium ions produced in a beam-foil experiment in which a subsurface positive muon beam of about 10 MeV/ c momentum passed through a thin metal foil. The formation of the muonium atoms was observed at various energies of the incident muon beam. Positive muons of a

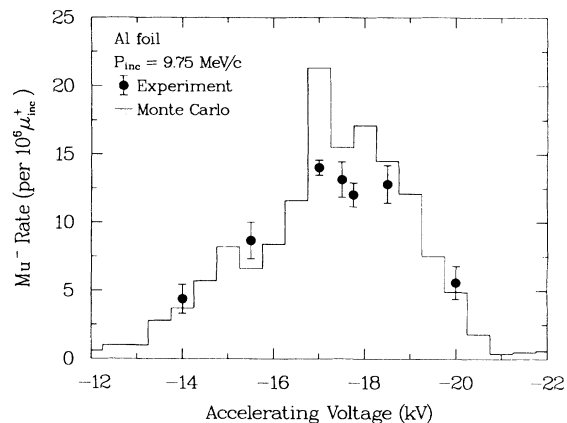


FIG. 14. Rates of negative muonium ions at the focal plane with Al foil. The solid circles with error bars represent projected rates based on time-of-flight data. The histogram corresponds to Monte Carlo simulations.

few keV to 20 keV coming out of the foils were also studied. A rate of $1.55(3) \times 10^{-4} / \mu_{\text{inc}}^+$, or 20 sec^{-1} , was observed for them with a momentum acceptance of $\Delta p/p = 8.5\%$ (FWHM).

The mass or the initial energy of the negative muonium ion was obtained by a time-of-flight technique. The mass of the ion is found to be $104 \pm 8 \text{ MeV}/c^2$, in good agreement with the expected value of $106.7 \text{ MeV}/c^2$ for Mu^- . The initial kinetic energy of the ion is in the vicinity of $0.2(1) \text{ keV}$. This is consistent with proton data and the velocity scaling rule. The lifetime of the ion is determined by the lifetime of the μ^+ . The decay process was also observed in the experiment by measuring the energy and time spectra of the decay positrons. The observed rate of the negative muonium ion at the spectrometer focal plane is about $10^{-5} / \mu_{\text{inc}}^+$ or 1.4 sec^{-1} (average). Since the production foils were placed in only moderately good vacuum ($3 \times 10^{-6} \text{ Torr}$), and the last several atomic layers of the foils are believed to play an important role in charge-capture processes, we cannot exclude effects from surface contamination. The formation fraction of the negative ions is expected to be the same for all foils. The slight difference in rates for Al, Be, and Au foils is likely caused by the different incident-beam conditions and the range of the muons in the different foils.

A Monte Carlo computer code was developed for this experiment. It can reproduce essentially all the experi-

TABLE IX. Projected formation fractions of negative muonium ions at the production foils. Errors, given in parentheses, are statistical only.

Foil	Thick.	Diam.	μ_{inc}^+		Mu ⁻ Rate at focal plane		Mu ⁻ Formation
			$p_{\mu_{\text{inc}}^+}$	Rate	$(10^{-5} / \mu_{\text{inc}}^+)$		prob. $(10^{-4} / \mu_{\text{inc}}^+)$
	(mg/cm ²)	(cm)	(MeV/ c)	(10^3 s^{-1})	Expt.	Monte Carlo	Monte Carlo
Be	4.6	7.6	12.63	145	0.57(11)	0.87	0.51
Al	0.2	7.6	9.75	129	1.40(6)	2.13	1.80
Au	3.8	6.4	10.67	146	1.46(13)	1.88	3.50

mental data within a factor of 2. The simulations were of substantial help in understanding the experimental data. The formation probabilities for the Mu^- at the foils are about $10^{-4}/\mu_{\text{inc}}^+$. The differences in Mu^- rates for different foils are also demonstrated in the Monte Carlo simulation. From a careful study of the energy and angular distributions of the particles leaving the foils, these differences can be understood in terms of the different stopping distributions of the muons for different foils. Studies of the low-energy positive muons leaving the foils indicate that the dE/dx is larger for high- Z material and the angular distribution is also wider. This is in agreement with general expectation.

The negative muonium ion itself is a very interesting system. A beam of such ions is now available for spectroscopy and atomic collision studies. An interesting experiment to measure the polarization of the ions is proposed.⁹ Since the Mu^- is a charged particle, a beam of neutral muonium atoms can be generated from a Mu^- beam through the process of stripping. Recently, advances have been made on a more intense muonium source in the thermal energy region.⁴²⁻⁴⁴ However, at present, muonium produced with the beam-foil method remains the only practical source of $2S$ -state muonium for Lamb-shift measurements. Therefore, more careful studies of a fast muonium source would be beneficial for future Lamb-shift experiments.

In the past it was often assumed that the angular distribution of the muonium atoms leaving a foil is isotropic because of a lack of experimental information. The Monte Carlo simulations developed for this experiment show that the angular distribution of the muonium atoms is considerably wider than that of muons, since the muonium atoms have lower energy than do the muons. One can take advantage of the characteristics of the angular distributions in Lamb-shift experiments by using muonium atoms that are produced at an angle to the beam axis. An investigation by us⁴⁵ of the angular distributions of the emerging muons and muonium atoms is in progress.

Although the present beam intensity for Mu^- is small ($\sim 1.4 \text{ sec}^{-1}$ average), increases up to a factor of 10 could be achieved by optimizing the incident μ^+ channel and the accelerator-spectrometer arrangement. It is well known that the charge-capture cross sections are larger for alkali-metal vapors and alkali-metal-coated targets. One would expect a factor of 10 or more increase in the formation of negative muonium ions using such targets.⁴⁵

The positive muons of a few keV energy can also be used for making $\text{Mu}(2S)$. One of the effective ways to produce $\text{H}(2S)$ is the following process:



The cross section of this process is measured⁴⁶ to be $10^{-15} - 10^{-14} \text{ cm}^2$ in the kinetic energy range from 5 to 10 keV for incident H^+ . With the current setup, a $\text{Mu}(2S)$ beam might be produced using the low-energy muons. The intensity of this $\text{Mu}(2S)$ beam would be about 0.02 s^{-1} , which is about an order of magnitude lower than that in the previous measurements of the muonium Lamb shift.⁶ A more intense source of low-energy positive

muons with small phase space is needed for a dramatic increase in intensity of $\text{Mu}(2S)$.

ACKNOWLEDGMENTS

We would like to thank Joseph C. Ivie, Seth E. Rislove, Richard D. Werbeck, and the LAMPF staff for help in constructing the apparatus. This work was funded in part by U. S. Department of Energy Grants No. DE-FG02-86ER40243 (Yale) and No. DE-FG02-84ER40146 (Syracuse), National Science Foundation Grant No. PHY85-17485 (William and Mary), and the Deutsche Forschungsgemeinschaft.

APPENDIX: ANALYSIS OF THE TIME-OF-FLIGHT SPECTRA

Because of the high counting rate in the muon counter, the TDC spectra are distorted. Clearly, the probability of recording a stop signal increases with decreasing time difference relative to the start signal. This effect can be seen in Fig. 8. The effect has been carefully studied by several authors.⁴⁷⁻⁴⁹ It is necessary to correct this rate effect in order to obtain the undistorted time-of-flight distribution, i.e., the distribution for correlated events.

One method to correct for this effect is to accept only those events for which there is no more than one stop signal in some optimized time window. Since there will be no second stop signal in this window, the rate effect will be generally reduced. However, there will be a compromise between the cleanness of the resultant spectrum and the overall efficiency of the time-of-flight spectrometer, since a wider window will result in a cleaner spectrum but fewer correlated counts in the spectrum. A time window, extending from channel 140 to channel 650, was set up to obtain clean time-of-flight spectra. It required having one and only one stop signal in this window. The spectrum for low-energy muons taken at a high voltage of 0.0 kV is shown in Fig. 10 as a histogram.

Another way to analyze the data is to study the relation between a TDC spectrum and an undistorted distribution. An undistorted distribution can be obtained if one can derive an analytical expression for the undistorted distribution based on the TDC spectrum, which is distorted. In order to do so, we consider the counting rate of a stop signal $R(t)$, as a function of time. We suppose that the counting process is purely Poisson-distributed. The probability that k stop pulses occur in a time interval from 0 to t is given by

$$P(k) = \frac{\left[\int_0^t R(\tau) d\tau \right]^k}{k!} \exp \left[- \int_0^t R(\tau) d\tau \right] . \quad (\text{A1})$$

Therefore, the probability that the first stop pulse occurs at time t is the same as the probability that none occurs in the time interval from 0 to t , i.e.,

$$P(0) = \exp \left[- \int_0^t R(\tau) d\tau \right] . \quad (\text{A2})$$

Hence, the TDC spectrum would be

$$M(t) = NR(t) \exp \left[- \int_0^t R(\tau) d\tau \right], \quad (\text{A3})$$

where N is the number of measurements, i.e., the number of start pulses in the TDC.

Let us consider the spectrum of STOP1 in which the first pulse of the stop counter is recorded. If a start signal is given by a pulse which is uncorrelated to the stop pulses (call it a type-I start), the probability density to have a stop at time t is

$$P_1^U(t) = Ue^{-Ut}, \quad (\text{A4})$$

using Eq. (A3), where U is the instantaneous counting rate of the detector used for the stop signal.

If a start signal is given by a pulse which is correlated with one of the pulses in the stop counter (call it a type-II start), there are two types of possible stop pulses in the STOP1 spectrum. Let us assume that $C(t)$ is the probability distribution of the correlated events, which is what we are mostly interested in. The probability density of having an uncorrelated stop in STOP1 spectrum with such a start is

$$P_1^{C1}(t) = Ue^{-Ut} \left[1 - \int_0^t C(\tau) d\tau \right], \quad (\text{A5})$$

while the probability density of having a correlated stop with such a start is

$$P_1^{C2}(t) = C(t)e^{-Ut}. \quad (\text{A6})$$

If we assume N such measurements and that there is one correlated pulse from the stop counter for each of the N_C measurements (type-II start), the TDC spectrum would be given by

$$M_1(t) = (N - N_C)Ue^{-Ut} + N_C Ue^{-Ut} \left[1 - \int_0^t C(\tau) d\tau \right] + N_C C(t)e^{-Ut}. \quad (\text{A7})$$

This can also be written as

$$M_1(t) = N \left[Ue^{-Ut} \left[1 - \int_0^t C'(\tau) d\tau \right] + C'(t)e^{-Ut} \right] \quad \text{with } C'(t) = \frac{N_C}{N} C(t). \quad (\text{A8})$$

The equation for $M_1(t)$ satisfies the normalization condition

$$\int_0^\infty M_1(t) dt = N. \quad (\text{A9})$$

$M_1(t)$ gives the STOP1 distribution of our experiment.

Equation (A8) will be used to derive the undistorted distribution of the time-of-flight spectrum. In principle, any one of the three TDC spectra can be used to extract the undistorted time-of-flight spectrum. The derivation of the expressions for STOP2 and STOP3 is given elsewhere.⁴⁰ However, in practice, the second and third spectra are complicated by the dead time of the electronic circuitry. We will therefore concentrate on the spectrum of STOP1.

The undistorted time-of-flight distribution is given by $N_C C(t)$. Equation (A8) can be rearranged as

$$N_C C(t) = NC'(t) = M_1(t)e^{Ut} - NU + U \int_0^t NC'(\tau) d\tau. \quad (\text{A10})$$

This equation can be regarded as an integral equation for $NC'(t)$. One method of solving the equation is to use an iteration method. We replace the integration in the equation by a summation, i.e.,

$$NC'(t_i) = M_1(t_i)e^{Ut_i} - NU + U \sum_{j=0}^i NC'(t_j)\Delta t, \quad (\text{A11})$$

where $t_j = j\Delta t$, $j = 0, 1, 2, \dots$. Equation (A11) is a good approximation of Eq. (A10) for very small Δt compared to the range of the TDC. Therefore we have

$$S(t_i) = \frac{1}{1 - U\Delta t} \left[M_1(t_i)e^{Ut_i} - NU + U \sum_{j=0}^{i-1} S(t_j)\Delta t \right], \quad (\text{A12})$$

where we have written $NC'(t_i)$ as $S(t_i)$, $M_1(t)$ is the TDC spectrum of STOP1, N is the total number of measurements (i.e., the number of start pulses). U is the instantaneous rate in the stop counter, which is on the order of $2.3 \times 10^6 \text{ sec}^{-1}$, and Δt is taken to be the time interval of one channel of the TDC, which is about 1 nsec.

For each spectrum, N is based on all the counts in the spectrum including overflow counts, and U is based on the counts in the muon counter and on the beam-gated running time recorded in the scalers for each spectrum. The origin of time is taken to be at channel 130 of the spectrum.

These are limitations for using Eq. (A12). First, the counting process of the stop counter has to satisfy Poisson statistics, and secondly U has to be constant. Since the errors are propagated, relatively large errors are introduced for data points having few counts.

*Present address: Robert Bosch GmbH, D-1000 Berlin 33, Federal Republic of Germany.

†Present address: Gesellschaft für Schwer-Ionen Forschung, Darmstadt, Federal Republic of Germany.

¹K. Allison, *Rev. Mod. Phys.* **30**, 1137 (1958).

²H. Tawara and A. Russek, *Rev. Mod. Phys.* **45**, 178 (1973).

³Robin Shakeshaft and Larry Spruch, *Rev. Mod. Phys.* **51**, 369 (1979).

⁴P. R. Bolton, A. Badertscher, P. O. Egan, C. J. Gardner, M. Gladisch, V. W. Hughes, D. C. Lu, M. Ritter, P. A. Souder, J. Vetter, G. zu Putlitz, M. Eckhause, and J. Kane, *Phys. Rev. Lett.* **47**, 1441 (1981).

⁵P. J. Oram, J. M. Bailey, P. W. Schmor, C. A. Fry, R. F. Kiefl, J. B. Warren, G. M. Marshall, and A. Olin, *Phys. Rev. Lett.* **52**, 910 (1984).

⁶A. Badertscher, S. Dhawan, P. O. Egan, V. H. Hughes, D. C.

- Lu, M. W. Ritter, K. A. Woodle, M. Gladisch, H. Orth, G. zu Putlitz, M. Eckhause, J. Kane, F. G. Mariam, and J. Reidy, *Phys. Rev. Lett.* **52**, 914 (1984).
- ⁷K.-P. Arnold, F. Chmely, M. Eckhause, M. Gladisch, V. W. Hughes, J. Kane, S. Kettell, Y. Kuang, K. Kumar, D. Lu, B. Ni, B. Matthias, H. Orth, R. Schaefer, P. Souder, K. Woodle, and G. zu Putlitz, *Bull. Am. Phys. Soc.* **31**, 35 (1986).
- ⁸D. R. Harshman, J. B. Warren, J. L. Beveridge, K. R. Kendall, R. F. Kiefl, C. J. Oram, A. P. Mills, Jr., W. S. Crane, A. S. Rupaal, and J. H. Turner, *Phys. Rev. Lett.* **56**, 2850 (1986).
- ⁹Y. Kuang, K.-P. Arnold, F. Chmely, M. Eckhause, V. W. Hughes, J. R. Kane, S. Kettell, D.-H. Kim, K. Kumar, D. C. Lu, B. Ni, B. Matthias, H. Orth, G. zu Putlitz, H. R. Schaefer, P. A. Souder, and K. Woodle, *Phys. Rev. A* **35**, 3172 (1987).
- ¹⁰H. Bethe and E. Salpeter, *Quantum Mechanics of One- and Two-Electron Atoms* (Plenum, New York, 1977).
- ¹¹H. S. W. Massey, E. H. Burhop, and H. B. Gilbody, *Electronic and Ionic Impact Phenomena*, 2nd ed. (Clarendon, Oxford, 1969), Vol. II.
- ¹²J. A. Phillips, *Phys. Rev.* **97**, 404 (1955).
- ¹³Klaus H. Berkner, Issas Bornstein, Robert V. Pyle, and J. Warrne Stearns, *Phys. Rev. A* **6**, 278 (1972).
- ¹⁴R. S. Bhattacharya, W. Eckstein, and H. Verbeek, *Surf. Sci.* **93**, 563 (1980).
- ¹⁵W. Eckstein and F. E. P. Matschke, *Phys. Rev. B* **14**, 3231 (1976).
- ¹⁶M. C. Cross, *Phys. Rev. B* **15**, 602 (1977).
- ¹⁷Werner Brandt, in *Atomic Collisions in Solids*, edited by S. Datz, B. R. Appleton, and C. D. Moak (Plenum, New York, 1975), Vol. 1, p. 261.
- ¹⁸Homer D. Hagstrum, *Phys. Rev.* **96**, 336 (1954).
- ¹⁹M. Kitagawa and Y. H. Ohtsuki, *Phys. Rev. B* **13**, 4682 (1976).
- ²⁰G. G. Ross and B. Terreault, *Nucl. Instrum. Methods B* **15**, 146 (1986).
- ²¹H. Verbeek, R. S. Bhattacharya, and W. Eckstein, *Surf. Sci.* **95**, 380 (1980).
- ²²Ming L. Yu, *Phys. Rev. Lett.* **40**, 574 (1978).
- ²³J. R. Hiskes, *J. Phys. (Paris) Colloq.* **40**, C7-179 (1979).
- ²⁴A. Badertscher, P. O. Egan, M. Gladisch, M. Greene, V. W. Hughes, F. G. Mariam, D. C. Lu, G. zu Putlitz, M. W. Ritter, P. A. Souder, and R. Werbeck, *Nucl. Instrum. Methods A* **238**, 200 (1985).
- ²⁵K. L. Brown, Stanford Linear Accelerator Center Report No. SLAC-75, 1967 (unpublished).
- ²⁶K. L. Brown, F. Rothacker, D. C. Carey, and Ch. Iselin, Stanford Linear Accelerator Center, Report No. SLAC-91, Rev. 2 UC-28, 1977 (unpublished).
- ²⁷Kim Allen Woodle, Ph.D. thesis, Yale University, 1985.
- ²⁸U. Fano, *Annu. Rev. Nucl. Sci.* **13**, 1 (1963).
- ²⁹J. Lindhard and M. Scharff, *Phys. Rev.* **124**, 128 (1961).
- ³⁰C. Varelas and J. P. Biersack, *Nucl. Instrum. Methods* **79**, 213 (1970).
- ³¹G. Molière, *Z. Naturforsch. Teil A* **2**, 133 (1947).
- ³²G. Molière, *Z. Naturforsch. Teil A* **3**, 78 (1948).
- ³³H. A. Bethe, *Phys. Rev.* **89**, 1256 (1953).
- ³⁴Morton Camac, *Rev. Sci. Instrum.* **22**, 197 (1951).
- ³⁵William G. Cross, *Rev. Sci. Instrum.* **22**, 717 (1951).
- ³⁶M. T. Menzel and H. K. Stokes, Los Alamos National Laboratory Report No. LA-UR-87-115, 1987 (unpublished).
- ³⁷John L. Warren, Mary T. Menzel, Grenfell Boicourt, Helen Stokes, and Richard K. Cooper, Los Alamos National Laboratory Report No. LA-UR-87-126, 1987 (unpublished).
- ³⁸E. B. Hughes, R. L. Ford, R. Hofstadter, L. H. O'Neill, R. F. Schilling, and R. J. Wedemeyer, *IEEE Trans. Nucl. Sci.* **NS-19**, 126 (1972).
- ³⁹Joseph Ladislav Wiza, *Nucl. Instrum. Methods* **162**, 587 (1979).
- ⁴⁰Yunan Kuang, Ph.D. thesis, Yale University, 1988.
- ⁴¹R. S. Gao, P. S. Gibner, J. H. Newman, K. A. Smith, and R. F. Stebbings, *Rev. Sci. Instrum.* **55**, 1756 (1984).
- ⁴²A. P. Mills, Jr., J. Imazato, S. Saitoh, A. Uedono, Y. Kawashima, and K. Nagamine, *Phys. Rev. Lett.* **56**, 1463 (1986).
- ⁴³G. A. Beer, G. M. Marshall, G. R. Mason, A. Olin, Z. Gelbart, K. R. Kendall, T. Bowen, P. G. Halverson, A. E. Pifer, C. A. Fry, J. B. Warren, and A. R. Kunselman, *Phys. Rev. Lett.* **57**, 671 (1986).
- ⁴⁴K. A. Woodle, K.-P. Arnold, M. Gladisch, J. Hofmann, M. Janousch, K. P. Jungmann, H.-J. Mundinger, G. zu Putlitz, J. Rosenkranz, W. Schäfer, G. Schiff, W. Schwarz, V. W. Hughes, and S. H. Kettell, *Z. Phys. D* **9**, 59 (1988).
- ⁴⁵K. W. Ehlers and K. N. Leung, *Rev. Sci. Instrum.* **51**, 721 (1980).
- ⁴⁶I. A. Sellin and L. Granoff, *Phys. Lett. A* **25**, 484 (1967).
- ⁴⁷M. Matoba, M. Hyakutake, H. Yamamoto, A. Katase, and M. Sonoda, *Nucl. Instrum. Methods* **94**, 199 (1971).
- ⁴⁸L. M. Lowe, J. F. Boulter, and W. V. Prestwich, *Nucl. Instrum. Methods* **105**, 461 (1972).
- ⁴⁹R. Hoffmann, G. Gaukler, G. Nolte, H. Schmidt-Böcking, and R. Schuch, *Nucl. Instrum. Methods* **197**, 391 (1982).